Journal of Sol-Gel Science and Technology
https://doi.org/10.1007/s10971-023-06197-5

ORIGINAL PAPER: DEVICES BASED ON SOL-GEL OR HYBRID MATERIALS

Selective and rapid detection of acetone using aluminum-doped zno-based sensors

Majdi Benamara[1] · Pedro Rivero-Antúnez[2] · Hassen Dahman[1] · Manel Essid[3] · Souhir Bouzidi[4] · Marc Debliquy[5] · Driss Lahem[6] · Víctor Morales-Flórez[2,7] · Luis Esquivias[2,7] · José P. B. Silva[8,9] · Lassaad El Mir[1]

Received: 31 March 2023 / Accepted: 19 July 2023

Abstract

We report the preparation and characterization of pure and doped ZnO nanoparticles with 1%, 3%, and 5% aluminum (AZO) using a sol-gel method followed by annealing at 400 °C for 2 h. The structural and morphological properties of the AZO nanoparticles were analyzed using X-ray Diffraction (XRD), Transmission Electron Microscopy (TEM) techniques, and Scanning Electron Microscopy (SEM) equipped with Energy Dispersive Spectrometry (EDS). Optical and specific area properties were investigated by photoluminescence (PL) and N_2 physisorption measurements. The results showed that pure and doped AZO nanoparticles crystallize under a hexagonal wurtzite structure and exhibit spherical shapes with nanometric dimensions. TEM and SEM images revealed that the pure and Al-doped ZnO were round nanoparticles with a size smaller that 100 nm. FTIR measurements were conducted to investigate the presence of Al-O stretching vibrations, which served as an indication of aluminum incorporation into the ZnO lattice. The results confirmed the successful integration of aluminum into the ZnO structure. Additionally, XPS measurements were performed to examine the elemental composition of the AZO samples. The presence of Zn 2p peaks in all AZO samples, along with the presence of Al 2p peaks in the Al-doped ZnO structures, provided further evidence for the successful incorporation of Al ions into the ZnO lattice. The PL spectra revealed the presence of various defects (oxygen vacancies, interstitials) in the structure of pure and doped ZnO. Moreover, we fabricated gas sensors by spray-coating the AZO nanoparticles on alumina substrates equipped with interdigitated gold electrodes. The sensors demonstrated linear responses to gas concentration in the range of 5 to 50 ppm, with high sensitivity and good reproducibility, particularly for A1ZO (1% Al-doped ZnO), which exhibited the highest response (~12) at 300 °C under 10 ppm of acetone. Furthermore, A1ZO demonstrated excellent selectivity to acetone compared to other volatile organic compounds (VOCs) gases. Our findings highlight the potential of aluminum-doped ZnO nanoparticles as a promising material for enhancing the sensing properties of acetone gas sensors.

✉ Majdi Benamara
majdibenamara1@gmail.com

✉ José P. B. Silva
josesilva@fisica.uminho.pt

[1] Laboratory of Physics of Materials and Nanomaterials Applied at Environment (LaPhyMNE), Faculty of Sciences in Gabes, Gabes University, 6072 Gabes, Tunisia

[2] Departamento de Física de la Materia Condensada, Universidad de Sevilla, 41012 Sevilla, Spain

[3] Chemistry Department, College of Science, King Khalid University (KKU), Abha, P.O. Box 9004, Saudi Arabia

[4] Laboratoire de la Matière Condensée et des Nanosciences, Département de Physique, Faculté des Sciences de Monastir, Avenue de l'Environnement Monastir, 5019 Monastir, Tunisia

[5] Service de Sciences des Matériaux, Université de Mons, Rue de l'Epargne 56, 7000 Mons, Belgium

[6] Materia Nova, Materials R&D Centre, Parc Initialis, Avenue Nicolas Copernic 3, 7000 Mons, Belgium

[7] Instituto de Ciencia de Materiales de Sevilla, Centro Mixto CSIC-Universidad de Sevilla, 41092 Sevilla, Spain

[8] Physics Center of Minho and Porto Universities (CF-UM-UP), University of Minho, Campus de Gualtar, 4710-057 Braga, Portugal

[9] Laboratory of Physics for Materials and Emergent Technologies, LapMET, University of Minho, 4710-057 Braga, Portugal

Published online: 05 August 2023

Graphical Abstract

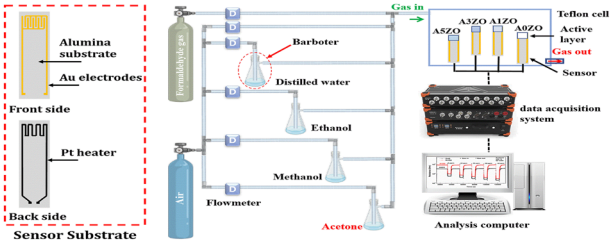

Keywords Volatile organic compounds sensors · Acetone selectivity · Aluminium doped ZnO nanoparticles

Highlights

- High sensitivity and reproducibility to acetone gas with 1% Aluminium-doped ZnO.
- Excellent response to acetone at low temperature (300 °C).
- Remarkable response to low acetone gas concentration.
- Good selectivity to acetone over other VOCs.
- Stable response under varying humidity levels.

1 Introduction

The technologies of today's industry and research frequently use organic liquids. Monitoring and quantifying the vapor concentration of these compounds in the air will be an important undertaking because most of them are extremely harmful to the environment and human health [1]. The volatile organic compounds (VOCs) in human breath, including acetone, ethanol, ammonia, methane, and pentane, act as diagnostic biomarkers for several disorders [2]. Individuals with uncontrolled diabetes or increased fat metabolism can exhibit elevated concentrations of acetone in their breath. Acetone is a metabolic byproduct that is produced when fat is broken down for energy instead of glucose, a condition known as ketosis. Uncontrolled diabetics, specifically those with diabetic ketoacidosis, often have high levels of acetone in their breath due to the inability to regulate glucose effectively. In normal healthy individuals, the typical range of acetone concentrations in breath varies from 0.3 to 4 parts per million (ppm) [3, 4]. However, when following a ketogenic diet, which involves consuming minimal carbohydrates and high amounts of fat, acetone concentrations in breath can significantly increase. Studies have shown that in adults on a ketogenic diet, breath acetone levels can reach as high as 40 ppm [5]. This increase in acetone concentration is attributed to the body's reliance on fat metabolism, leading to the production of ketones, including acetone, as an alternative energy source. Monitoring acetone levels in breath becomes particularly important in assessing the effectiveness of dietary interventions and managing metabolic conditions. Applications requiring excellent selectivity and low concentration (some ppm level) of acetone detection will be needed. Due to its poor selectivity and low acetone sensitivity, pure zinc oxide is rarely used to detect acetone gas. There are numerous ways to enhance sensing capabilities, including designing microstructures [6], controlling defects [7], creating p-n junctions [8], and altering precious metals [9].

Chemical sensors built on semiconductor metal oxide (MOS) are advantageous because of their small size, high sensitivity, low cost, ability to be integrated into portable analyzers, and usefulness in the detection of acetone in exhaled air. Most sensor materials, including In_2O_3, SnO_2, Fe_2O_3, TiO_2, ZnO, WO_3, Co_3O_4, and others, offer good gas detection characteristics for each gas (reducing or oxidizing). In particular, there are reports that chemoresistive sensors based on MOS materials such as Fe_2O_3 [10], SnO_2 [11], WO_3 [12], and ZnO [13] have been employed for the detection of acetone while other VOCs can also be detected. Due to its intriguing features and multiple uses in solar cells, electronics, gas sensors, and optoelectronics, zinc oxide, with n-type II-VI semiconductor material and a high exciton binding energy of 60 meV and a broadband gap of 337 eV, has drawn a lot of attention [14, 15]. In addition, ZnO is one of the most desirable metallic oxides because of its relatively easy manufacturing, excellent thermal conductivity, and chemical stability. The number of surface sites accessible for gas interaction, the energy band structure, the particle shape, and the crystal structure of ZnO can all affect the detection characteristics of the material. According to Li et al. [16], the ZnO nanowall gas sensor exhibits outstanding acetone vapor detection capability with a high response value, quick recovery time, and strong selectivity. Doping semiconductors with metal oxides is a significant and successful way to

enhance gas detection capabilities [17]. In fact, the improving of the selectivity, sensitivity, and stability of gas sensors was doing by doping with noble metals (Pt, Pd) or other additions like Cu and Al [18, 19]. By altering the energy band, structure, and morphology of the nanoparticles, adding additional gas interaction centers to the semiconducting surface of the metal oxide, and raising the surface/volume ratio, these dopants enhance the gas detection characteristics. Doping ZnO with aluminum can improve the gas detection properties, according to Hjiri et al. [20]. According to Yoo et al. [21], Al doping can enhance the ZnO nanopowders (NPs) nanostructure, optical, and gas sensing characteristics for acetone detection. Doping ZnO with Al increased the detection features, such as strong detection response, quick response/recovery times, good stability, and high selectivity, according to Koo et al. [22]. The literature suggests that ZnO sensors generally demonstrate enhanced sensitivity to acetone at elevated temperatures. The temperature range of 200 to 400 °C is frequently considered suitable for VOC gas detection in general, and specifically for acetone gas, as it promotes improved gas adsorption and desorption kinetics, thereby enhancing the sensing performance [23]. At these temperatures, both pure and doped ZnO-based sensors can effectively interact with VOC molecules, including acetone, facilitating their adsorption onto the sensor surface and leading to measurable changes in electrical properties [24]. Many techniques, including auto-combustion, sol-gel [25], co-precipitation, thermal stock [26], laser ablation in liquid [27], hydrothermal [28], and the sonochemical method [29], were used to create pure and doped ZnO nanoparticles. The sol-gel method is one of them, and it has a minimum equipment requirement and reaction temperature. On the other hand, it enables the production of materials with a high degree of purity, crystallinity, and a variety of shapes [30].

In this work, we investigate the sensing performance of AZO (Aluminum-doped ZnO) materials with varying Al loadings to optimize the effect of Al on the selectivity enhancement of ZnO nanoparticles for acetone sensing. We show that the different Al loadings significantly changes the sensing properties of ZnO-based gas sensors, particularly in detecting acetone gas. The mechanisms for sensing acetone with Aluminum-doped ZnO are unraveled and a better understanding of the optimal Al concentration that can enhance the selectivity of ZnO nanoparticles towards acetone is provided.

2 Samples preparation

2.1 Nanoparticles synthesis

Zinc oxide doped with aluminum nanopowders was prepared using a sol-gel route with 16 g of zinc acetate dehydrated [$Zn(CH_3COO)_2.2H_2O$;99%] as a precursor in 112 ml of methanol. After magnetically stirring at room temperature for 10 min, an adequate amount of aluminum nitrate-9-hydrate corresponding to the [Al/Zn] ratio of 0, 0.01, 0.03, and 0,05 was added. After 15 min of magnetic stirring, the solution was placed in an autoclave and dried in a supercritical condition of ethyl alcohol (EtOH) ($T_c = 243$ °C, $P_c = 63.6$ bar). Furthermore, the obtained nanopowders were annealed at 400 °C in the air for 2 h. Samples are indicated as A0ZO, A1ZO, A3ZO, and A5ZO for [Al]/[Zn] ratios of 0, 0.01, 0.03, and 0.05, respectively. Figure 1a shows the basic steps of the preparation protocol used by the sol-gel route.

2.2 Sensor fabrication and sensing test

The prepared nanopowders (250 mg) were mixed in 2.25 ml of distilled water. This solution was sonicated using an ultrasonic of xW power for 15 min until a uniformly dispersed solution was obtained. The solution is then sprayed on interdigitated gold electrodes printed on alumina (Al_2O_3) substrates (C-MAC Micro Technology Company, Belgium), presented in the Fig. 1b. To stabilize the deposited film and obtain a stable electrical signal, the sensors were calcined in air for 1 h at 400 °C before sensing tests.

Detection tests were performed in a homemade gas detection measurement system. The gas system, presented in Fig. 1c, contains a Teflon chamber enclosing the prepared sensors which were related to a data acquisition system to operate the sensors at a controlled temperature and perform resistance measurements while varying the concentration of the target gas. The electrical system was connected to computer to treat the obtained results. There are also two gas cylinders (Formaldehyde and air) controlled by debitmeters and related to the Teflon cell. Four barboters contain distilled water and dilute aqueous solutions of ethanol, methanol, and acetone to provide humidity and targets gases concentrations in the sensing cell.

The gas sensing performances were carried out by measuring the variation in electrical resistance between the air and the target gas. Before the test, commercial synthetic air (79% N_2 + 21% O_2) was injected into the chamber until the electrical resistance stabilized. After that, acetone gas was introduced into the chamber to obtain the desired concentration of 5, 10, 20, 30, and 50 ppm, which take 15 min of injection time, and then the acetone gas was removed. These tests were performed at 50% humidity by bubbling the gas in distilled water. The gas response was defined as the ratio $R = (R_{air} - R_{gas})/R_{gas}$, where R_{air} and R_{gas} are the electrical resistance at 50% humidity of the sensor in air and at different concentrations of acetone gas, respectively. Response/recovery times were evaluated at 90% resistance change after exposure to target gas and air.

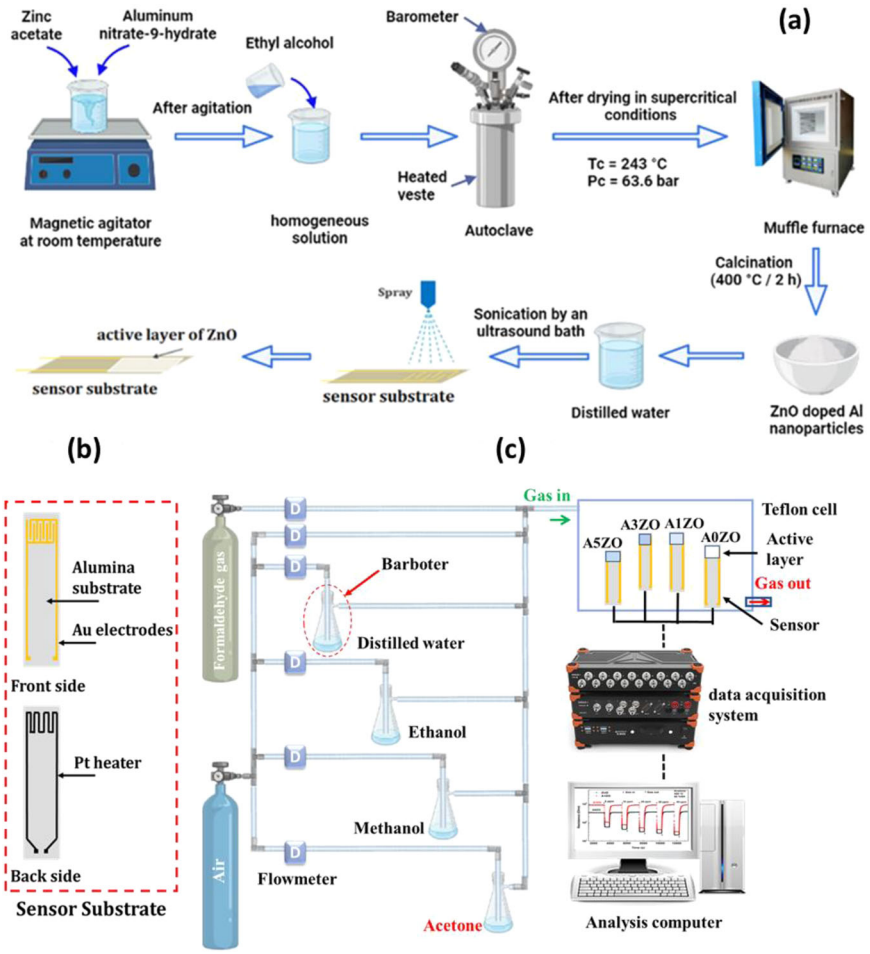

Fig. 1 **a** Sol-gel protocol nanoparticle synthesis and sensor fabrication. **b** sensor substrate and **c** Sensing device

To ensure stable and accurate sensing experiments, precautions were taken regarding the high-temperature range and its impact on the Teflon material and testing environment. During the experiments, the sensor was heated to the desired temperature range of 200–350 °C while maintaining a safe distance from the Teflon cell to avoid any direct contact. To address any potential temperature-related issues, the testing environment within the Teflon cell was carefully controlled. In both the air and gas injection processes, measures were implemented to cool the environment inside the cell, ensuring that the high temperature did not adversely affect the Teflon material or interfere with the stability of the sensing experiments. These precautions allowed for reliable and consistent data collection without compromising the integrity of the experimental setup or the accuracy of the results.

2.3 Characterization

The crystal structure and particle size were investigated by X-ray diffraction (XRD, Bruker AXS D8 Advance) and measurements. The Fourier-transform infrared spectroscopy (FT-IR) analysis was performed using a BRUKER IFS 66 v/s FTIR spectrometer. The spectrometer's scanning range spanned from 3000 to 450 cm^{-1}, and the FT-IR operated in absorbance mode, allowing for precise measurements of sample characteristics. XPS experiments were conducted using a PHOIBOS HSA3500 MCD-9 device with normal emission configuration. The photoemission spectra were analyzed by fitting them with a convoluted Gaussian and Lorentzian function. The morphologies of the prepared nanoparticles and deposited layers were obtained by transmission electron microscopy (TEM) and scanning electron microscopy (SEM). TEM was performed with a JEOL JEM 2010 electron microscope (LaB6 electron gun) equipped with a Gatan 794 Multi-Scan CCD camera and operating at 200 kV. SEM, equipped with EDX, measurement was investigated by field-emission scanning electron microscopy (FE-SEM, S4800II, Hitachi, Japan). To obtain the optical properties, a modular NanoLog Horiba spectrofluorometer (Horiba, Kyoto, Japan) was used for PL measurements and was equipped with a Xe lamp as an excitation light source with a wavelength of 325 nm at room temperature. Emissions were examined between 350 and 800 nm. The nanostructural features of the samples were investigated by N_2-physisorption experiments (Micromeritics ASAP2010

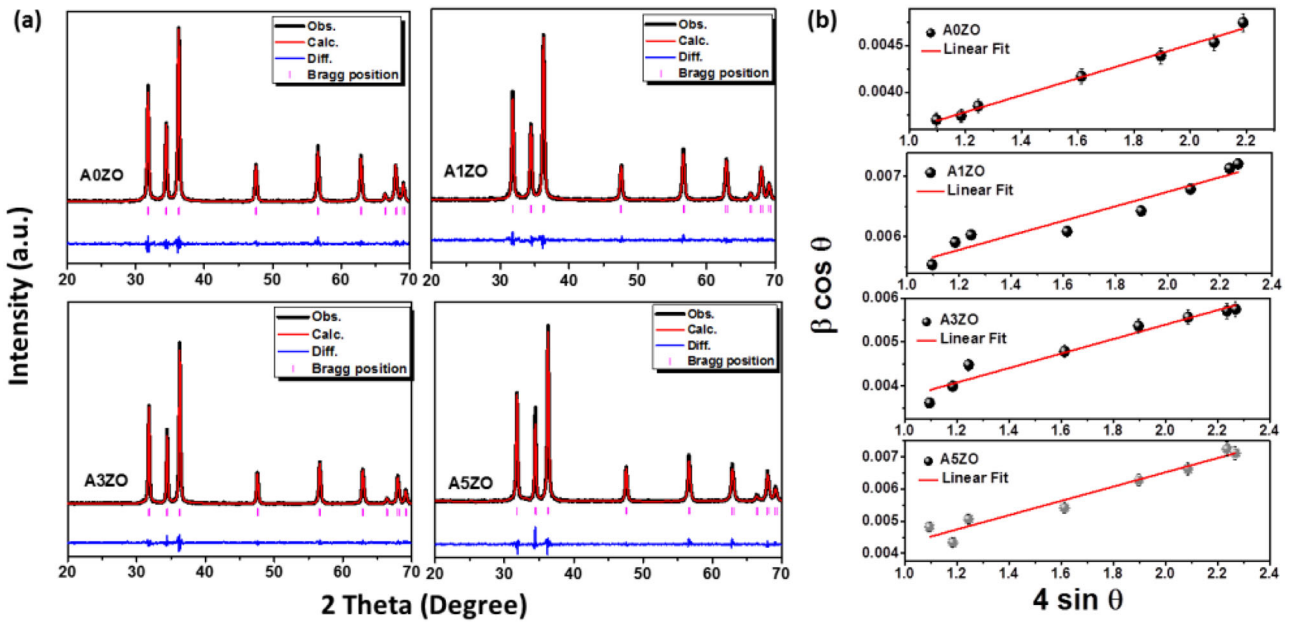

Fig. 2 **a** Rietveld refined X-ray diffraction patterns, and **b** Williams-Hall plots of the AZO samples

operating at 77 K and equipped with a pressure transducer with a resolution of 10^{-4} mm Hg). Before to the N_2 physisorption analyses, the samples were degassed at 150 °C for 2 h under a flow of N_2. Specific surface area, specific pore volume, pore size, and pore size distribution (PSD) were determined using standard models for analysis (BET and BJH, respectively).

3 Results and discussions

3.1 Microstructure and morphological investigations

In Fig. 2a, the Rietveld refinement analysis was carried out with the aid of the full proof program further the X-ray diffraction patterns of the AZO nanoparticles. The indexed peaks indicate that pure and doped ZnO crystallizes under hexagonal wurtzite structure with space group P63mc, according to JCPDS card no. 01-073-8765. The XRD plots of the Al-doped ZnO nanoparticles do not exhibit any additional peaks, indicating the successful substitution of Al^{3+} ions for Zn^{2+} ions. Previous studies have shown that introducing a small amount of Al into ZnO does not alter the structural phase of hexagonal ZnO, and no extra peaks corresponding to other materials are observed [31, 32]. Therefore, the XRD analysis confirms the synthesis of pure phases of ZnO and Al-doped ZnO nanoparticles using the sol-gel method. Table 1 contains the calculated and listed values of the various structural parameters. The average crystallite size and lattice strain of the AZO samples were calculated using Williamson-Hall (W-H) plots which are represented in the Fig. 2b. Those graphs were plotted by representing βcosθ vs. of 4sinθ, from which we can provide the strain from the slope of the linear fit of the curves and the mean crystallite size (D_{WH}) from their intercept. The lattice parameters (a and c) can be calculated from the two peaks according to the miller indices (100) and (002). Consequently, the volume of the unit cell can be concluded through the following relationships:

$$a = \frac{\lambda}{\sqrt{3}\sin\theta_{(100)}} \quad (1)$$

$$c = \frac{\lambda}{\sin\theta_{(002)}} \quad (2)$$

$$V = 0.866 * a^2 * c \quad (3)$$

The density of the AZO samples can be calculated considering that the basic unit cell of the wurtzite hexagonal structure contained strong ions using the following equation:

$$\rho_{XRD} = \frac{2.M}{N_A.V} \quad (4)$$

Where M, N_A, and V represent molecular weight, Avogadro's number, and volume, respectively. 2 is the number of molecules in a unit cell of wurtzite hexagonal structure. From the calculated X-ray density, assuming all nanoparticles are spherical, the specific surface area (S_{XRD})

Table 1 Structural parameters of the AZO samples, specific surface area and particle size. pore volume, Vp, and diameter of the AZO samples estimated by BET and BJH methods, and particle diameter (d_{BET})

Parameters	A0ZO	A1ZO	A3ZO	A5ZO
a (Å)	3.244 ± 0.001	3.246 ± 0.001	3.245 ± 0.001	3.245 ± 0.001
c (Å)	5.195 ± 0.002	5.201 ± 0.002	5.200 ± 0.002	5.199 ± 0.002
V ($Å^3$)	47.338 ± 0.003	47.465 ± 0.003	47.431 ± 0.003	47.423 ± 0.003
$D_{W\text{-}H}$ (nm)	52	32	66	69
ε (10^{-4})	9.1 ± 0.1	12.0 ± 0.1	16.5 ± 0.2	22.2 ± 0.2
R_p (%)	6.360 ± 0.002	6.170 ± 0.003	7.160 ± 0.002	7.850 ± 0.002
R_{wp} (%)	8.490 ± 0.002	9.730 ± 0.003	9.780 ± 0.002	10.300 ± 0.002
X^2	1.478 ± 0.005	1.463 ± 0.006	1.478 ± 0.005	1.502 ± 0.008
ρ_{XRD} ($g.cm^{-3}$)	5.709 ± 0.002	5.694 ± 0.001	5.698 ± 0.002	5.699 ± 0.002
S_{XRD} (m^2/g)	20.211 ± 0.005	32.929 ± 0.008	15.954 ± 0.004	15.258 ± 0.005
D_{TEM} (nm)	38	29	35	45
S_{BET} (m^2/g)	13.1472 ± 0.0002	15.3574 ± 0.0003	22.5749 ± 0.0003	27.2586 ± 0.0003
d_{BET} (nm)	80	68	47	39
Vp (cm^2/g)	0.112109 ± 4E-6	0.084392 ± 2E-6	0.105325 ± 3E-6	0.091366 ± 2E-6
Pore diameter (nm)	36.1 ± 0.3	24.0 ± 0.2	20.1 ± 0.1	15.3 ± 0.1

can be estimated from the following relationship:

$$S_{XRD} = \frac{6000}{D.\rho_{XRD}} \quad (5)$$

where 6000 is the spherical particles factor and D is the particle diameter calculated from W-H plots.

Table 1 presents the structural parameters of AZO samples which are similar to the standard parameters of zinc oxide in the hexagonal wurtzite structure according to Garcia-Martinez et al. [33]. As can be seen, the specific surface area varied in the range 15.258 and 32.929, in which it was higher for Al-doped ZnO than the pure sample, exceptionally in the A1ZO. However, it is important to note that the high value of the specific surface area of the samples is necessary to improve gas detection applications.

The Fig. 3a displays the FTIR spectra of pure and Al-doped ZnO samples. The observed peaks in these spectra originate from various sources. In the pure ZnO structure, the peak at 879 cm^{-1} corresponds to Zn-O stretching vibrations, which are characteristic of zinc oxide. Peaks at 1963, 2062, and 2161 cm^{-1} in the pure and Al doped ZnO spectra may be associated with impurities or defects in the ZnO lattice, potentially influenced by carbon-related interactions from the zinc acetate precursor. Introduction of carbon species during synthesis can create localized defects or form carbon-oxygen bonds within the ZnO structure, resulting in additional peaks. The peak at 2631 cm^{-1} is attributed to the stretching vibrations of surface-adsorbed water molecules. The broad band around 3433 cm^{-1} in the FTIR spectra of Al-doped ZnO samples indicates the presence of a stretching vibration related to hydroxyl (OH) groups [34]. This suggests the existence of surface hydroxyl species or the adsorption of water molecules onto the ZnO surface. With the addition of Al, a high-intensity peak around 671 cm^{-1} emerges, corresponding to Al-O stretching vibrations, indicating the incorporation of aluminum into the ZnO lattice [35]. This alteration in the chemical composition due to the introduction of aluminum leads to changes in the electronic structure and the creation of new vibrational modes. The intense peak at 671 cm^{-1} indicates a strong interaction between aluminum and oxygen atoms, enhancing chemical bonding and localizing aluminum within the ZnO matrix. These observed peaks, including the high-intensity peak at 671 cm^{-1} in the Al-doped ZnO spectra, demonstrate the structural and chemical modifications resulting from the doping process.

X-ray photoelectron spectroscopy (XPS) analysis was conducted to investigate the elemental chemical states and confirm the presence and incorporation of aluminum (Al) during the sol-gel process. The obtained binding energies from the XPS analysis were adjusted for specimen charging by referencing the C 1s peak at 284.6 eV. In Fig. 3b, the Zn 2p1/2 and Zn 2p3/2 core levels of the A0ZO sample were centered at 1041.9 eV and 1018.9 eV, respectively, with a spin-orbit splitting of 23 eV, which is consistent with other ZnO architectures [36, 37]. Similarly, A1ZO, A3ZO, and A5ZO exhibited comparable peaks, but with slightly lower binding energies, indicating the incorporation of Al into the ZnO lattice. This downward shift in binding energy can be attributed to the lower electronegativity of Al, which screens the Zn electron cloud [38]. Figure 3c illustrates the Al 2p core level spectra of the A1ZO, A3ZO, and A5ZO samples, revealing a shift of the Al 2p with increasing the Al concentration from 73.7 eV up to 74.5 eV. As expected, no discernible signal was detected for the pure sample (A0ZO). These observations provide strong evidence for the presence and successful integration of Al ions into the ZnO lattice. The area ratio between Al 2p and Zn 2p for the A1ZO, A3ZO, and

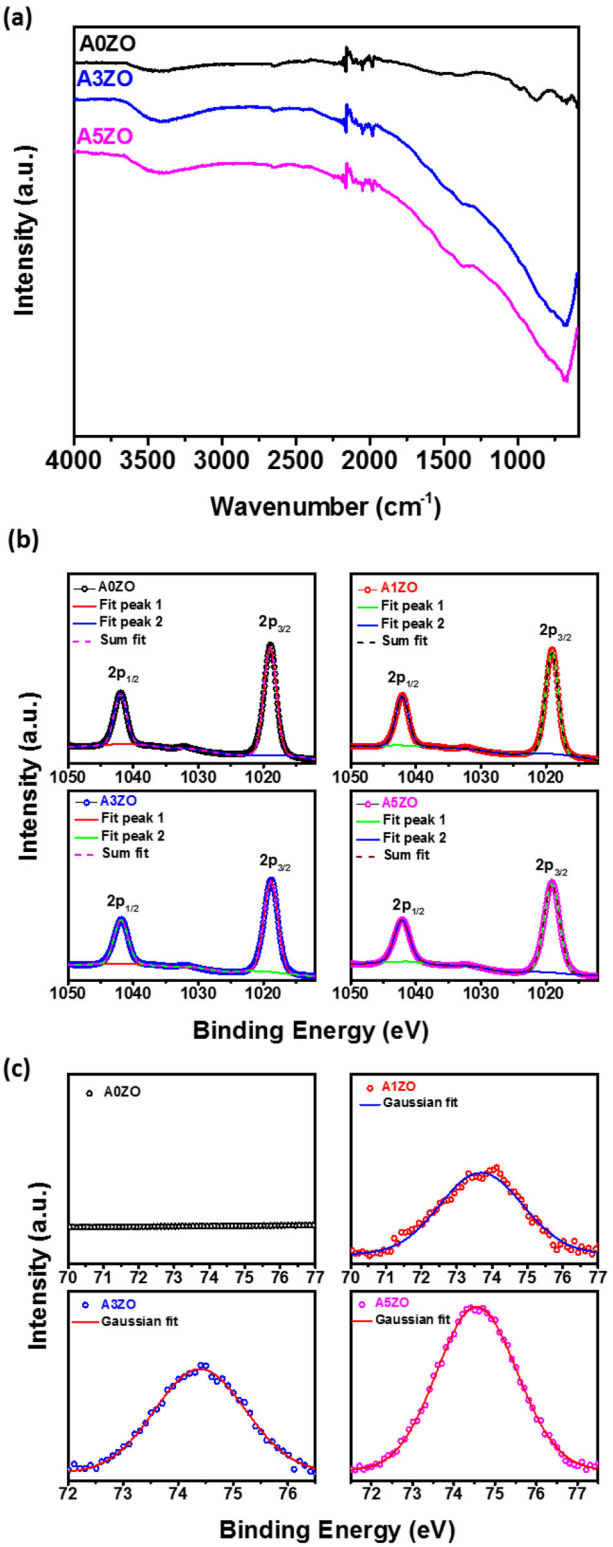

Fig. 3 **a** FTIR spectra of the pure and Al doped ZnO. XPS spectra of **b** Zn 2p, and **c** Al 2p of the different AZO nanoparticles

A5ZO samples was determined to be 0.026, 0.035, and 0.066, respectively. These findings indicate a gradual increase in the concentration of Al within the prepared samples.

Figure 4 presented TEM images of particle shape for pure and Al-doped ZnO samples. The grain sizes were less than 100 nm for all samples. By comparing the ZnO and Al-doped ZnO samples, we have seen that the A1ZO particle sizes were smaller than those of pure zinc oxide. The grain size distribution of the AZO samples indicate that the A1ZO sample size has the lowest value than the other valid interpretations of the samples given by XRD measurements.

In addition, the morphology of ZnO and A3ZO samples has been studied by SEM, which is shown in Fig. 5a, b, respectively. We can see the presence of round nanoparticles with an average size less than 100 nm for both samples. It is clear from this images that the grain size of ZnO powders is larger than that of A3ZO, which was the highest surface area. However, it is interesting to note that the high surface area of nanoparticles is necessary for sensing applications [39–41]. Furthermore, the EDX spectra for both samples were studied and are shown in the same figures (Fig. 5a, b). It indicates the presence of many peaks at different intensities. For undoped ZnO, we have investigated two peaks referred to Zn and O indicating that the purity of zinc oxide and the percentage of the Zn and O elements was 53.5% and 46.5%, respectively. The A3ZO sample contains the elements Zn, O and Al in percentages values 50.9, 46.7 and 3.3%, respectively. The presence of the Al element at 3.3 %, which is close to 3 %, indicates the correct percentage of desired doping.

3.2 N_2 physisorption measurement

The Brunauer-Emmet-Teller (BET) adsorption-desorption isotherms of pure and Al-doped ZnO samples produced via sol-gel are shown in Fig. 6. According to IUPAC, the registered isotherms are of type II. Clustered particles with a mesoporous architecture and unrestrained monolayer-multilayer adsorption have an H_3-type hysteresis loop. Because of the Al incorporation, the surface areas of Al-doped ZnO NPs are greater than those of pure ZnO NPs. The projected SBET rises nearly four orders of magnitude, from 13.1472 $m^2.g^{-1}$ for pure ZnO to 27.2586 $m^2.g^{-1}$ for a 5 percent Al component (Table 1). In addition, the pore diameter and volume are 15.3–36.1 nm and 0.084392–0.112109 $cm^3.g^{-1}$, respectively. The aggregation of the particles may be linked to the reduction in both volume and diameter of the pores. The average particle diameter (d_{BET}) may be calculated using the following formula:

$$d_{BET} = \frac{6000}{S_{BET} \times \rho} \tag{6}$$

Where the terms S_{BET} ($m^2.g^{-1}$) and ρ ($g.cm^{-3}$) represent the calculated BET specific surface area and material density, respectively. The value of the particle diameter resulting from the surface area is given in Table 1.

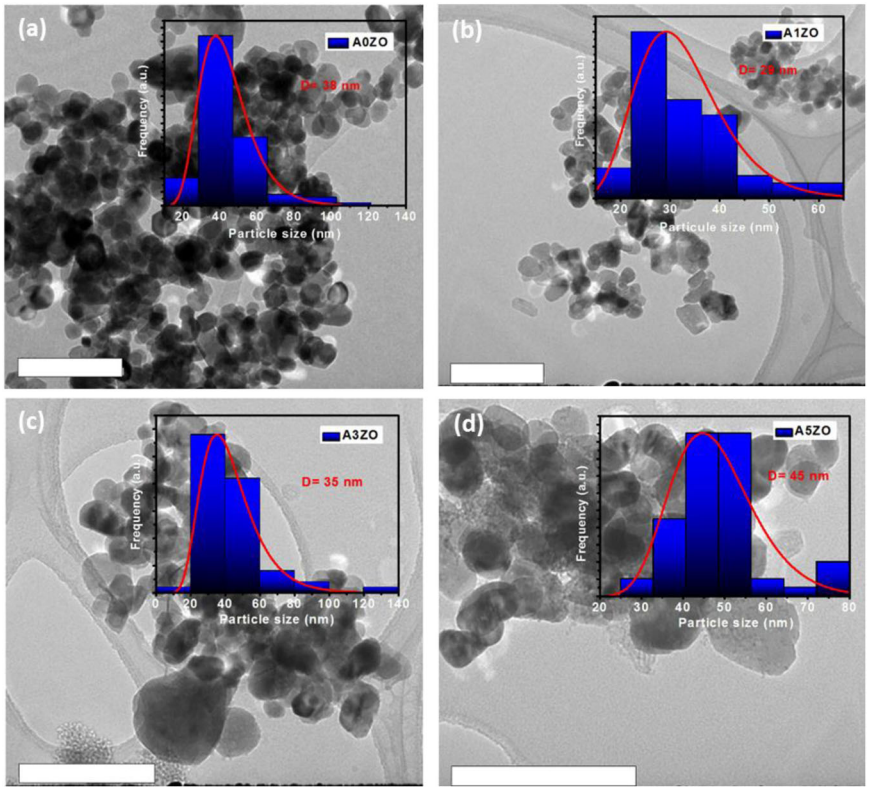

Fig. 4 TEM pictures and frequencies vs particle size of **a** A0ZO, **b** A1ZO, **c** A3ZO, and **d** A5ZO samples (200 nm scale)

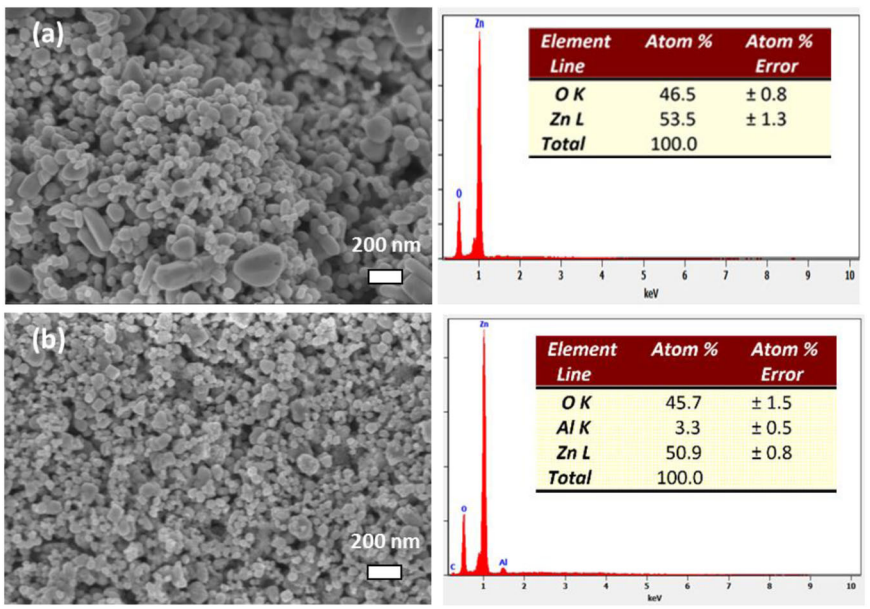

Fig. 5 SEM-EDX images of **a** ZnO and **b** A3ZO samples

3.3 PL measurements

The PL spectra of AZO nanoparticles are presented in Fig. 7. The PL spectrum of pure ZnO showed the presence of two bands, a narrow band in the UV emission and a broad band in the visible emission. The UV emission refers to band-band emission and the visible band is attributed to the defects present in the inter-band. The wide band present in the visible range referred to several defects, such as interstitial zinc (Zn_i), oxygen antisites (O_{Zn}), and oxygen vacancies (V_o) [42, 43]. With a comparison between Al-doped ZnO and pure ZnO PL spectra, the green emission intensity band gradually disappeared, and the UV emission band increased in intensity. There is a new band that appeared at 437 nm, which it was

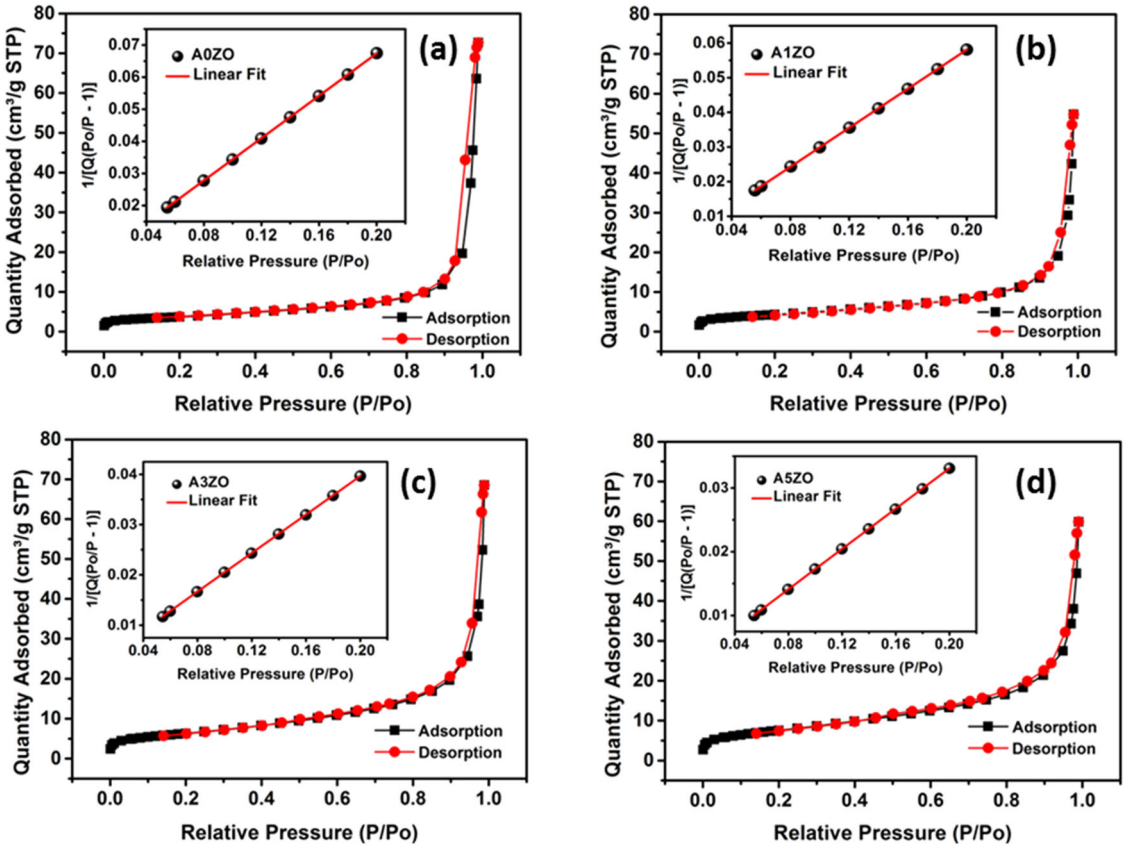

Fig. 6 N_2 adsorption/desorption curves at 77 K for **a** A0ZO, **b** A1ZO, **c** A3ZO, and **d** A5ZO

attributed to the blue emission from intrinsic defects and due to the recombination between the donor-acceptor pair related to the acceptor of the Al element.

The PL spectra of AZO samples were deconvoluted by Gaussian fit. The Fig. 7a–d show the deconvolution of the Gaussian curve for the experimental PL spectrum of A0ZO, A1ZO, A3ZO, and A5ZO nanopowders, respectively. The Gaussian fit of the experimental PL measurement identifies many emission peaks centered at 382 nm (3.25 eV), 460 nm (2.69 eV), 493 nm (2.52 eV), 553 nm (2.24 eV), 651 nm (1.90 eV) and 730 nm (1.69 eV), respectively. The blue emission peaks centered on 2.69 and 2.52 eV are affected by the transition from interstitial zinc (Zn_i) to the valence band and zinc vacancy (V_{Zn}), respectively [42, 43]. The green emission peak centered at 2.24 eV is attributed to conduction band transitions to the antisite oxygen (O_{Zn}). The orange-red emission peaks centered at 1.90 eV and 1.69 eV are attributed to the conduction band transition to oxygen vacancy (V_o) and oxygen interstitial (O_i), respectively [44, 45].

3.4 Acetone sensing tests

The sensing tests were performed for the pure and Al-doped ZnO samples. Firstly, we have performed the resistance as a function of temperature, shown in Fig. 8a, of AZO samples under air. The resistance under air decreased when the operating temperature was increased. Under air, oxygen species were adsorbed by the ZnO surface. At low temperatures (at 200 and 250 °C), most of the adsorbed species are O^-. At high operating temperatures (at 300 and 350 °C), most of the adsorbed oxygen species are O^{2-}. Furthermore, the electrical potential is inversely proportional to the operating temperature [18]. This behavior is explained by the fact that the bound electrons become free electrons if they are given enough energy which can be thermal. The electrons stripped from atoms become charge carriers, which can then conduct current and subsequently cause a decrease in resistance. The higher electrical resistance observed in the A1ZO sample compared to the undoped, A3ZO, and A5ZO samples can be attributed to the smaller particle size of A1ZO as determined from TEM images presented in Fig. 4. Smaller particle size results in an increased number of grain boundaries and interfaces within the material, leading to enhanced scattering and electron-electron interactions. These effects hinder the flow of electric current, ultimately resulting in higher electrical resistance.

The sensing properties of AZO samples towards the detection of acetone (C_3H_6O) at low concentrations (5–50 ppm) in the air with 50% of humidity were initially

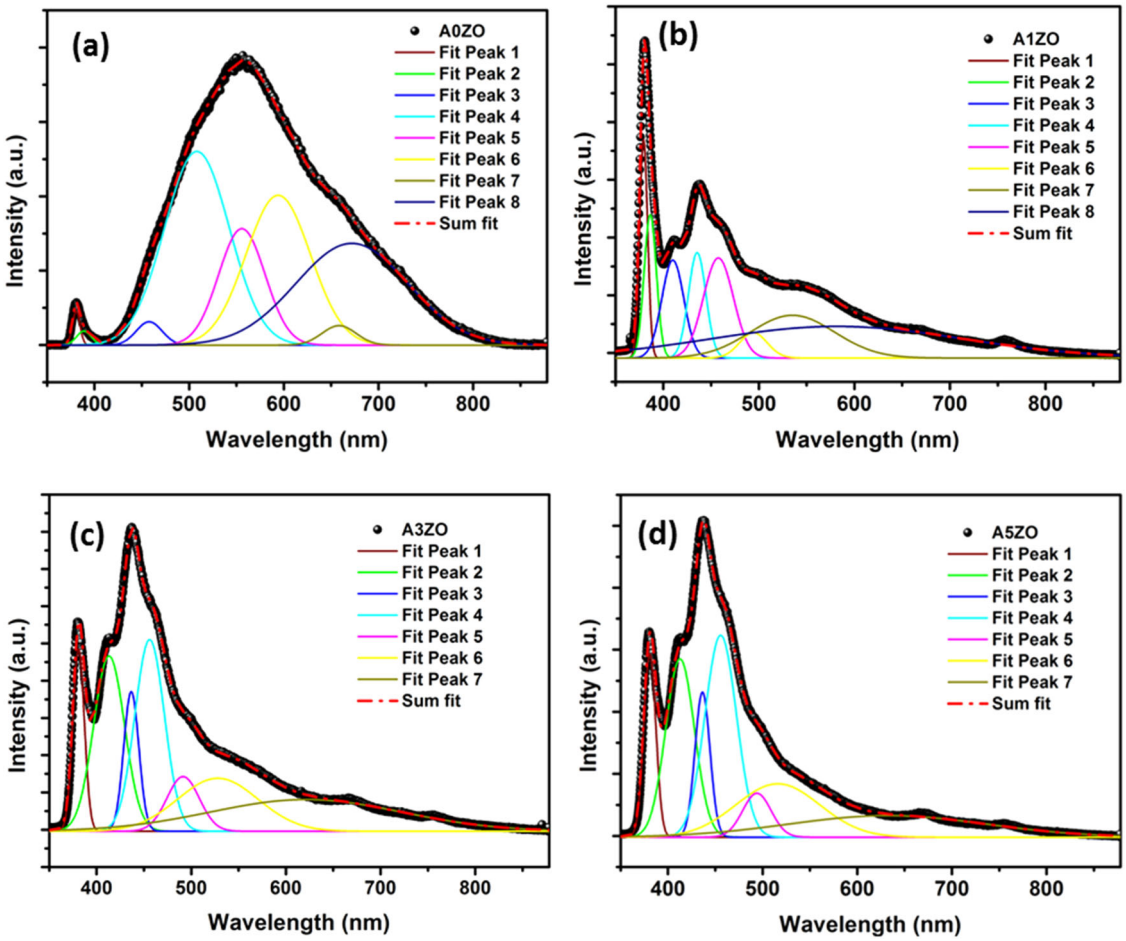

Fig. 7 Room temperature PL spectra with sub-peak positions and contents from Gaussian decomposition of **a** ZnO, **b** A1ZO, **c** A3ZO, and **d** A5ZO

investigated at different operating temperatures. The responses versus temperature of the fabricated sensors, which were tested at 10 ppm of acetone concentration, are reported in Fig. 8b. The Al-doped ZnO samples have a strongly favorable sensitivity, compared to undoped ZnO sample, toward acetone gas. However, some differences can be noticed depending on the Al content and operating temperature. The response/recovery times were estimated from the base resistance variation of the AZO samples, presented in Fig. 8c, under air and acetone gas, respectively.

At 300 °C, the best sensitivity was obtained with the lowest Al loading, so we can use the A1ZO sensor and ZnO sensor as a reference. All the sensors under investigation presented a reduction in resistance when acetone was added which it was showing that Al doping preserves the n-type semiconductor features of undoped ZnO. We have investigated the resistances versus time of A1ZO and pure ZnO under different concentrations of acetone at the operating temperature (300 °C), shown in Fig. 9a.

Acetone injection induced a remarkable variation in the electrical resistance of the detection layer. We have seen the variation of the sensor response as a function of time which is extracted following the equation [22]:

$$\text{Response} = \left(R_{air} - R_{gas}\right)/R_{air} \quad (7)$$

in which R_{air} is the resistance under air and R_{gas} is the resistance under gas. Figure 9b shows the time response of A1ZO and pure ZnO under different concentrations at 300 °C. A1ZO sensor has more responsive than pure zinc oxide. The addition of Al in the zinc oxide has increased the surface area of this behavior which may explain the increase in sensor response. Both sensors have linear responses as a function of acetone concentrations.

The gas detection process of an Al-doped ZnO sensor involves gas molecules adsorbing and desorbing on the detection material's surface, causing a change in resistance. Oxygen molecules in the air adsorb on the surface of the material, creating O_2^-, O^-, or O^{2-} ions by capturing electrons in the conduction band [46, 47]. This lowers the density of free charge carriers, increasing the depletion region and raising the resistance of NP ZnO. The ionized species O_2^-, O^-, and O^{2-} are prominent at temperatures

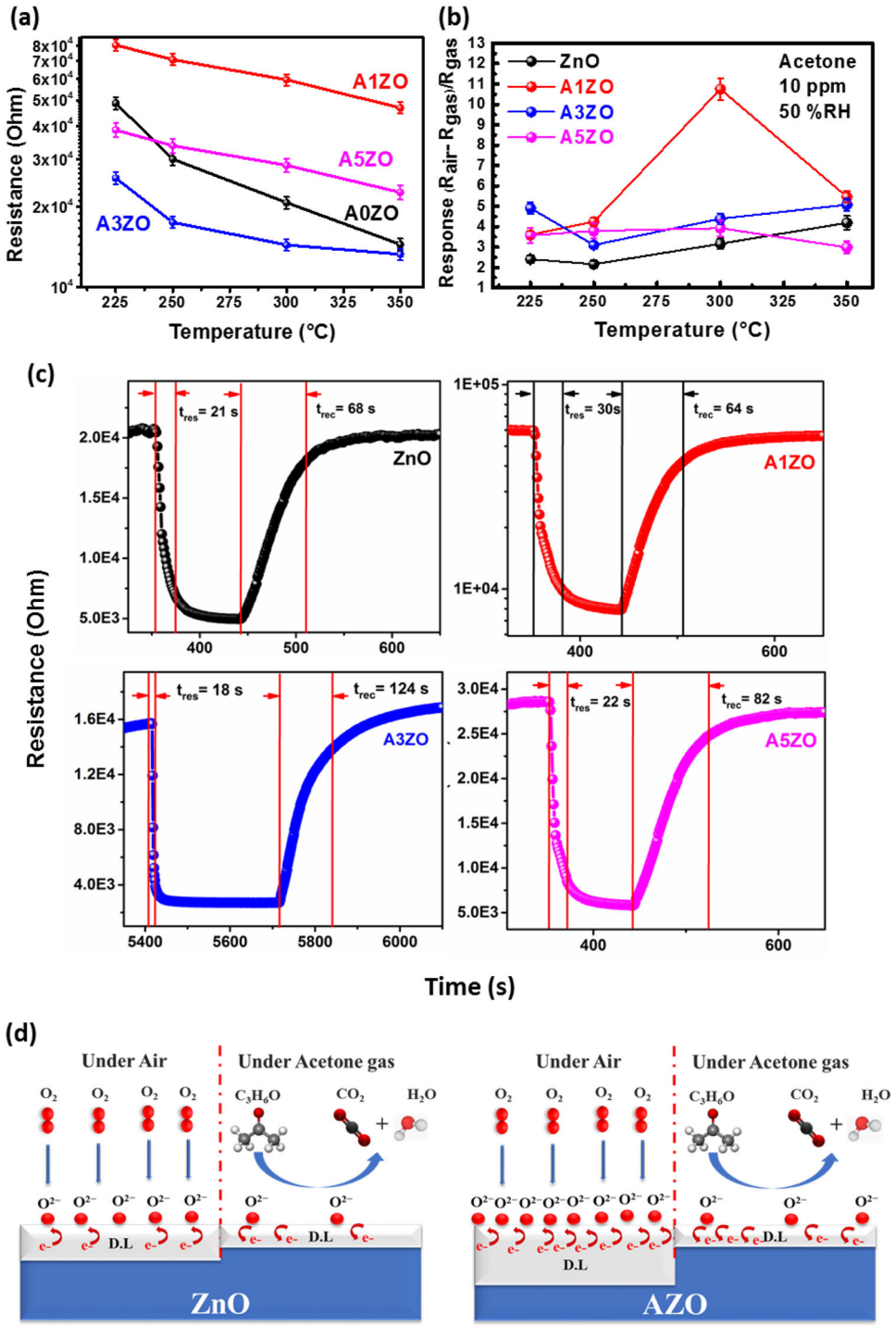

Fig. 8 **a** Base resistance as a function of temperature under air. **b** Sensor responses vs temperature for ZnO, A1ZO, A3ZO and A5ZO under 10 ppm of acetone. **c** Base resistance vs. time of AZO samples at 300 °C. **d** Sensing mechanism of pure and doped ZnO under air and under acetone gas

below 150 °C, between 150 and 400 °C, and above 400 °C, respectively [48]. When a few ppm of gas is injected, the acetone molecules react with the oxygen species on the ZnO surface, producing CO_2 and H_2O and releasing trapped electrons in the conduction band. This results in a sudden decrease in resistance [49–51]. The A1ZO sensor has improved responsiveness due to its smaller size and greater specific area, which enhances the concentration of adsorbed species. Additionally, oxygen vacancies act as adsorption sites to enhance gas detection ability. This results in the percolation channel broadening and the electron-depleted layer shrinking, but the flow of electrons is unaffected. The detecting process is further explained in Fig. 8d.

Figure 9c illustrates the repeatability of ZnO and A1ZO sensors in response to 10 ppm acetone vapor at 300 °C. The sensors show consistent responses over four successive

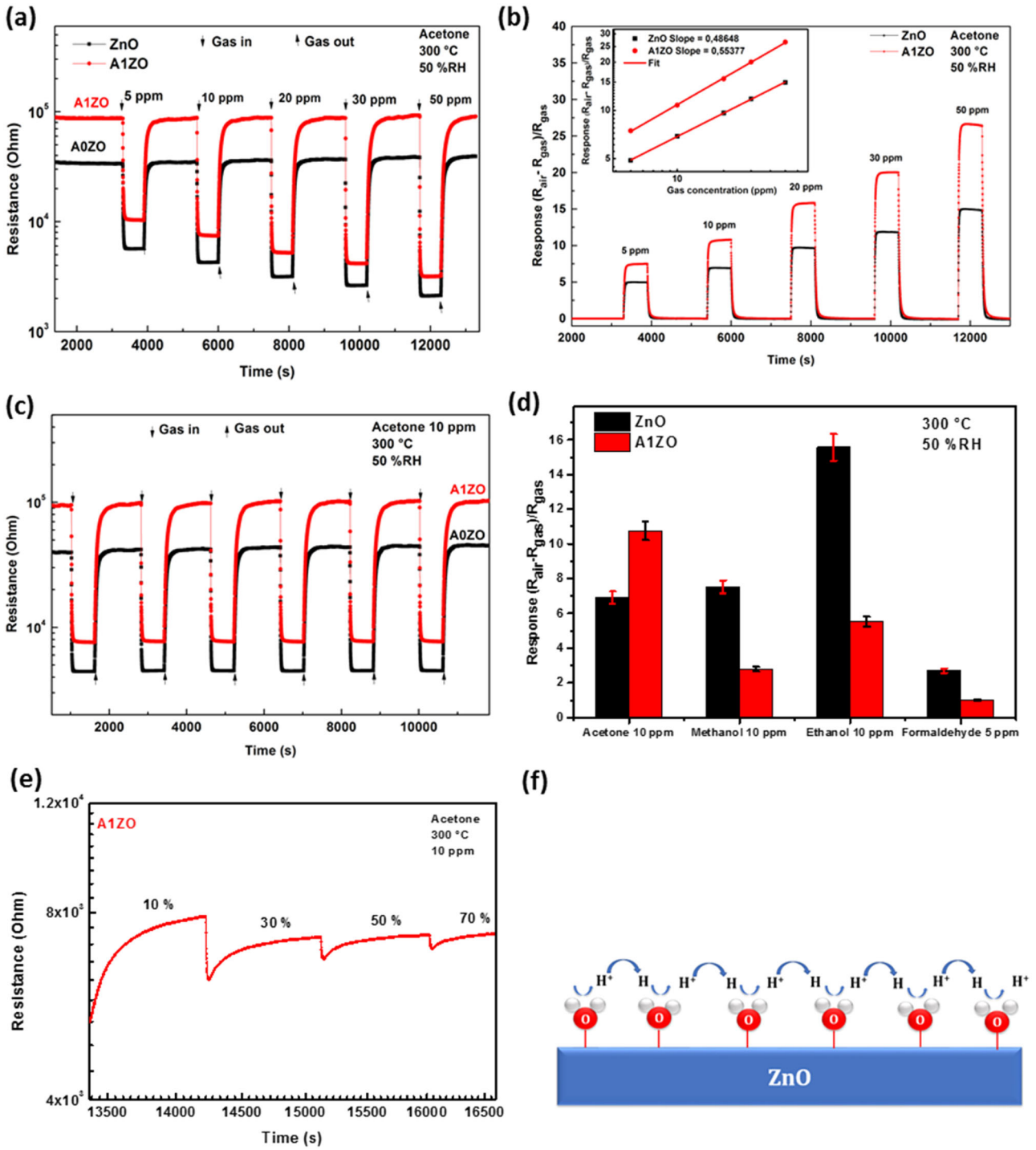

Fig. 9 **a** Sensor resistance and **b** sensor responses vs time for ZnO and A1ZO under different concentration of acetone gas at 300 °C. **c** Reliability of ZnO and A1ZO in sensing 10 ppm acetone over 6 cycles at 300 °C. **d** Sensor response of ZnO and A1ZO for 10 ppm of various target gases such as acetone, methanol, ethanol, and formaldehyde at 300 °C. **e** Sensor resistance in the different relative humidity percentages (from 10 to 70%RH) under 10 ppm of acetone gas concentration. **f** Principle of adsorption of H_2O molecules in the surface

sensing cycles, indicating good repeatability. Figure 9d shows the sensor responses of A1ZO and ZnO to different gases at 300 °C. A1ZO sensor shows higher response to acetone vapor compared to formaldehyde, ethanol, and methanol, indicating good selectivity. The dipole moment difference between the gases may be the reason for the A1ZO sensor's selectivity. Figure 9e shows the base resistance of the A1ZO sensor under 10 ppm of acetone gas

Table 2 Comparison acetone responses between ZnO doped Al and other materials

Materials	Sensing temperature	Acetone concentration (ppm)	Responses	References
$ZnO/ZnCo_2O_4$ nanocomposites	275 °C	100	7.5	[52]
ZnO/GO	450 °C	200	12.52	[46]
Co-doped ZnO	360 °C	100	16	[53]
ZnO rods	300 °C	100	4.5	[48]
Ag/ZnO nanocomposites	250 °C	100	15	[49]
ZnO nanoplates	450 °C	125	20	[50]
Al doped ZnO	300 °C	50	27	This work

concentration at different humidity levels (10%, 30%, 50%, and 70%). As relative humidity increased, the sensor initially experienced a rapid decrease in resistance, followed by an exponential increase. This behavior is attributed to the interaction between adsorbed water molecules and the sensor's surface. At lower humidity levels, water molecules adsorb onto the surface, enhancing conductivity and significantly reducing resistance. However, as humidity further rises, the thicker water layer acts as a barrier, limiting the interaction between acetone gas and the sensor, resulting in decreased response and an exponential increase in resistance. These findings highlight the sensor's sensitivity to humidity changes and its stability in maintaining consistent electrical properties and response characteristics. The ZnO doped Al sensor exhibits promising potential for accurate and reliable gas sensing applications, particularly in environments with varying humidity levels. Additionally, Fig. 9f illustrates the moisture detection mechanism, showcasing the interplay between the sensor's membrane and the adsorption/desorption of water molecules. The sensor's resistance remaining relatively unchanged underscores its high stability, indicating minimal influence from humidity fluctuations, which further emphasizes the robustness and reliability of the ZnO doped Al sensor in maintaining its sensing capabilities under various environmental conditions.

Table 2 illustrates the superior acetone-sensing performance of our home-made sol-gel derived $Al_{1\%}$-doped ZnO nanoparticles compared to various other materials. When compared to $ZnO/ZnCo_2O_4$, ZnO/GO, Co-doped ZnO, Ag/ZnO nanocomposites, ZnO rods, and porous ZnO nanoplates, our Al-doped ZnO nanoparticles exhibit significantly enhanced sensitivity to acetone gas, which makes promising the present Aluminum-doped ZnO nanoparticles for sensing.

4 Conclusion

A sol-gel approach was used to make aluminum-doped ZnO powders with various Al loadings. The prepared samples were investigated as an acetone gas detection layer after annealing at 400 °C. The morphologies, crystallite sizes, and microstructure of all doped and undoped samples, as a function of Al loading, revealed a hexagonal wurtzite structure with crystallite sizes of approximately 60 nm, as validated by SEM images. Then, at an ideal operating temperature of 300 °C, we studied the acetone sensing capabilities of pure and 1 percent Al-doped ZnO, which revealed an excellent sensing response of 11 and a response time of 17 s for the detection of 10 ppm acetone. Al-doped ZnO has greater sensing characteristics than pure ZnO. Al-doped ZnO's improved detection performance opens up a wide range of applications, including environmental and industrial monitoring systems, as well as breath analyzers for monitoring personal health problems.

Acknowledgements The authors extend their appreciation to the Deanship of Scientific Research at King Khalid University for funding this work through a large group Research Project under grant number RGP2/110/44.

Author contributions MB: Conceptualization, Methodology, Investigation, Formal analysis, Writing – original draft. PR-A: Methodology & Investigation. HD: Methodology, Investigation, Supervision. ME: review & editing. SB: Rietveld refinement. MD: Resources, Methodology. DL: Conceptualization, Writing – review & editing, Supervision, Funding acquisition. VM-F: Formal analysis, Writing – review & editing, Resources. LE: Formal analysis, Review & editing, Resources. JPBS: XPS analyses, Review & editing. LEM: Conceptualization, Methodology, Investigation, Formal analysis, Supervision.

Funding This work is financially supported by the Tunisian Ministry of Higher Education and Scientific Research (PRF 2019-D4P2), the European Regional Development Fund (ERDF), and the Walloon Region of Belgium through the Interreg V France-Wallonie-Vlaanderen program, under PATHACOV project, and the Micro + project co-funded by the European Regional Development Fund (ERDF) and Wallonia, Belgium (No. 675781-642409). In addition, this work was supported by the Portuguese Foundation for Science and Technology (FCT) in the framework of the Strategic Funding Contract UIDB/04650/2020. J.P.B.S. also expresses gratitude to FCT for the contract under the Institutional Call to Scientific Employment Stimulus – 2021 Call (CEECINST/00018/2021).

Compliance with ethical standards

Conflict of interest The authors declare no competing interests.

References

1. Iben Nassar K, Rammeh N, Soreto Teixeira S, Graça MPF (2022) Physical Properties, Complex Impedance, and Electrical Conductivity of Double Perovskite $LaBa_{0.5}Ag_{0.5}FeMnO_6$. J Electron Mater 51(1):370–377
2. Benamara M, Massoudi J, Dahman H, Dhahri E, El Mir L, Ly A, Lahem D (2020) High response to sub-ppm level of NO_2 with 50% RH of ZnO sensor obtained by an auto-combustion method. J Mater Sci Mater Electron 31(17):14249–14260
3. Spanel P, Dryahina K, Rejskova A, Chippendale TWE, Smithm D (2011) Breath acetone concentration; biological variability and the influence of diet. Physiol Meas 32:23–31
4. Anderson JC, Lamm WJE, Hlastala MP (2006) Measuring airway exchange of endogenous acetone using a single-exhalation breathing maneuver. J Appl Physiol 100:880–889
5. Anderson JC (2015) Measuring breath acetone for monitoring fat loss. Obesity 23:2327–2334
6. Wang LL, Chen S, Li W, Wang K, Lou Z, Shen G (2019) Grain-boundary-induced drastic sensing performance enhancement of polycrystalline-microwire printed gas sensors. Adv Mater 31:1804583
7. Wang WC, Liu FQ, Wang B, Wang Q (2019) Reduced graphene oxide-porous In_2O_3 nanocubes hybrid nanocomposites for room-temperature NH_3 sensing. Chin Chem Lett. 30:1261–1265
8. Deng L, Bao L, Xu J, Wang D, Wang X (2020) Highly sensitive acetone gas sensor based on ultra-low content bimetallic PtCu modified $WO_3{\cdot}H_2O$ hollow sphere. Chin Chem Lett 31(8):2041–2044
9. Xu DS, Xu PC, Wang XQ, Chen Y, Yu H, Zheng D, Li X (2020) Pentagram-Shaped Ag@ Pt Core–Shell Nanostructures as High-Performance Catalysts for Formaldehyde Detection. ACS Appl Mater Interf 12:8091–8097
10. Benamara M, Zahmouli N, Soreto Teixeira S, Graça MPF, El Mir L, Valente MA (2022) Electrical and Magnetic Studies of Maghemite (γ-Fe_2O_3) Prepared by the Sol–Gel Route. J Electron Mater 51(5):2698–2707
11. Singkammo S, Wisitsoraat A, Sriprachuabwong C, Tuantranont A, Phanichphant S, Liewhiran C (2015) Electrolytically Exfoliated Graphene-Loaded Flame-Made Ni-Doped SnO_2 Composite Film for Acetone Sensing. ACS Appl Mater Interf 7:3077–3092
12. Wang L, Teleki A, Pratsinis SE, Gouma PI (2008) Ferroelectric WO_3 Nanoparticles for Acetone Selective Detection. Chem Mater 20:4794–4796
13. Darvishnejad MH, Firooz AA, Beheshtian J, Khodadadi AA (2016) Highly sensitive and selective ethanol and acetone gas sensors by adding some dopants (Mn, Fe, Co, Ni) onto hexagonal ZnO plates. RSC Adv 6:7838–7845
14. Palanisamy S, Ezhil Vilian AT, Chen SM (2012) Direct electrochemistry of glucose oxidase at reduced graphene oxide/zinc oxide composite modified electrode for glucose sensor. Int J Electrochem Sci 7:2153–2163
15. Yang K, She GW, Wang H, Ou XM, Zhang XH, Lee CS, Lee ST (2009) ZnO nanotube arrays as biosensors for glucose. J Phys Chem C 113:20169–20172
16. Li SM, Zhang LX, Zhu MY, Ji GJ, Zhao LX, Yin J, Bie LJ (2017) Acetone sensing of ZnO nanosheets synthesized using room-temperature precipitation. Sens. Actuators B Chem 249:611–623
17. Kohl D (1990) The role of noble metals in the chemistry of solid-state gas sensors. Sens Actuators B Chem 1:158–165
18. Trivikrama Rao GS, Tarakarama Rao D (1999) Gas sensitivity of ZnO based thick film sensor to NH_3 at room temperature. Sens Actuators B Chem 55:166–169
19. Yang Z, Huang Y, Chen G, Guo Z, Cheng S, Huang S (2009) Ethanol gas sensor based on Al-doped ZnO nanomaterial with many gas diffusing channels. Sens. Actuators B Chem 140:549–556
20. Iben Nassar K, Slimi M, Rammeh N, Bouhamed A, Njeh A, Kanoun O (2021) Investigation of AC electrical conductivity and dielectric properties of $BiBaFeZnO_6$ double perovskite oxides. J Mater Sci: Mater Electron 32:24050–24057
21. Yoo R, Güntner AT, Park Y, Rim HJ, Lee HS, Lee W (2019) Sensing of acetone by Al-doped ZnO. Sens Actuators B Chem 283:107–115
22. Koo A, Yoo R, Woo SP, Lee HS, Lee W (2019) Enhanced acetone-sensing properties of Pt-decorated Al-doped ZnO nanoparticles. Sens Actuators B Chem 280:109–119
23. Rath RJ, Farajikhah S, Oveissi F, Dehghani F, Naficy S (2023) Chemiresistive Sensor Arrays for Gas/Volatile Organic Compounds Monitoring: A Review. Adv Eng Mater 25(3):2200830
24. Epping R, Koch M (2023) On-Site Detection of Volatile Organic Compounds (VOCs). Molecules 28(4):1598
25. El Ghoul J, Omri K, El Mir L, Barthou C, Alaya S (2012) Sol-gel synthesis and luminescence properties of SiO_2/Zn_2SiO_4 and SiO_2/Zn_2SiO_4:V composite materials. J Lumin 132:2288
26. Rajput P, Vashishtha P, Gupta G, Kamni (2021) A comparative study on structural and optical properties of ZnO nanoparticles prepared by three different synthesis methods. Mater Today Proc 43:3856–3861
27. Nguyen HTP, Nguyen TMT, Hoang CN, Le TK, Lund T, Huynh TKX (2020) Characterization and photocatalytic activity of new photocatalysts based on Ag, F-modified ZnO nanoparticles prepared by thermal shock method. Arab J Chem 13:1837–1847
28. Anugrahwidya R, Yudasari N, Tahir D (2019) Optical and structural investigation of synthesis ZnO/Ag Nanoparticles prepared by laser ablation in liquid. Mater Sci Semicond Process 105:104712
29. Taha KK, Modwi A, Elamin M, Arasheed R, Al-Fahad AJ, Albutairi I, Arasheed H, Alfaify M, Anojaidi K, Algethami FK (2019) Impact of Hibiscus extract on the structural and activity of sonochemically fabricated ZnO nanoparticles. J Photochem Photobiol A Chem 390:112263
30. Benamara M, Zahmouli N, Kallekh A, Bouzidi S, El Mir L, Alamri HR, Valente MA (2023) Study of the magnetic properties of Mg, Gd, and Co doped maghemite (γ-Fe_2O_3) nanoparticles prepared by sol–gel. J Magn Magn Mater 569:170479
31. Ahammed N, Hassan MS, Hassan M (2018) Effects of aluminum (Al) incorporation on structural, optical and thermal properties of ZnO nanoparticles. Mater Sci -Pol 36 3:419–426
32. Jantrasee S, Moontragoon P, Pinitsoontorn S (2016) Thermoelectric properties of Al-doped ZnO: experiment and simulation. J. Semicond. 37(9):092002
33. Garcia-Martinez O, Rojas RM, Vila E, De JM (1993) Vidales, Microstructural characterization of nanocrystals of ZnO and CuO obtained from basic salts. Solid State Ion 63:442–449
34. Vayssilov GN, Aleksandrov HA, Dib E, Costa IM, Nesterenko N, Mintova S (2022) Superacidity and spectral signatures of hydroxyl groups in zeolites. Microporous Mesoporous Mater 343:112144
35. Tong Y, Wirth J, Kirsch H, Wolf M, Saalfrank P, Campen RK (2015) Optically probing Al—O and O—H vibrations to characterize water adsorption and surface reconstruction on α-alumina: An experimental and theoretical study. Chem Phys 142(5):054704
36. Benamara M, Massoudi J, Dahman H, Ly A, Dhahri E, Debliquy M, El Mir L, Lahem D (2021) Study of room temperature NO_2

sensing performances of ZnO_{1-x} (x = 0, 0.05, 0.10). App Physics A 128(1):1–18
37. Bembibre A, Benamara M, Hjiri M, Gómez E, Alamri HR, Dhahri R, Serra A (2022) Visible-light driven sonophotocatalytic removal of tetracycline using Ca-doped ZnO nanoparticles. J Chem Eng 427:132006
38. Islam MN, Ghosh TB, Chopra KL, Acharya HN (1996) XPS and X-ray diffraction studies of aluminum-doped zinc oxide transparent conducting films. Thin Solid Films 280(1-2):20–25
39. Benamara M, Teixeira SS, Graça MPF, Valente MA, Jakka SK, Dahman H, Dhahri E, Debliquy M, Lahem D (2021) Study of ZnO room temperature NO_2 sensor under illumination prepared by auto-combustion. App Physics A 127(9):1–15
40. Neher SH, Klein H, Kuhs WF (2018) Determination of crystal size distributions in alumina ceramics by a novel X-ray diffraction procedure. J Am Ceram Soc 101:1381–1392
41. Benamara M, Bouzidi S, Zahmouli N, Teixeira SS, Graça MPF, El Mir L, Valente MA (2022) Electrical transport of Mg-doped maghemite (γ-Fe_2O_3) nanoparticles. App Physics A 128(7):1–15
42. Yatskiv R, Grym J (2016) Luminescence properties of hydrothermally grown ZnO nanorods. Superlattices Microstruct 99:214–220
43. Chand P, Gaur A, Kumar A, Gaur UK (2015) Effect of NaOH molar concentration on optical and ferroelectric properties of ZnO nanostructures. Appl Surf Sci 356:438–446
44. Mannam R, Kumar ES, Priyadarshini DM, Bellarmine F, Gupta ND, Rao MSR (2017) Enhanced photoluminescence and heterojunction characteristics of pulsed laser deposited ZnO nanostructures. Appl Surf Sci 418:335–339
45. Soylu M, Coskun M (2018) Controlling the properties of ZnO thin films by varying precursor concentration. J Alloys Compd 741:957–968
46. Egashira M, Kanehara N, Shimizu Y, Iwanaga H (1989) Gas-sensing characteristics of Li^+-doped and undoped ZnO whiskers. Sens Actuators B Chem 18:349–360
47. Shimizu Y, Kai S, Takao Y, Hyodo T, Egashira M (2000) Correlation between methylmercaptan gas-sensing properties and its surface chemistry of SnO2-based sensor materials. Sens Actuators B Chem 65:349–357
48. Ahn MW, Park KS, Heo JH, Park JG, Kim DW, Choi KJ, Lee JH, Hong SH (2008) Improvement of acetone gas sensing performance of ZnO nanoparticles. Appl Phys Lett 93:26310301–26310303
49. Hu J, Zou C, Su Y, Li M, Han Y, Kong ES-W, Yang Z, Zhang Y (2018) An ultrasensitive NO_2 gas sensor based on a hierarchical Cu_2O/CuO mesocrystal nanoflower. J Mater Chem A 6:17120–17131
50. Al-Hardan NH, Abdullah MJ, Aziz AA (2013) Performance of Cr-doped ZnO for acetone sensing. Appl Surf Sci 270:480–485
51. An W, Wu X, Zeng XC (2008) Adsorption of O_2, H_2, CO, NH_3, and NO_2 on ZnO Nanotube: A Density Functional Theory Study. J Phys Chem C 112:5747–5755
52. Duy LV, Duy NV, Hung CM, Hoa ND, Dich NQ, (2020) Urea mediated synthesis and acetone-sensing properties of ultrathin porous ZnO nanoplates. Mater Today Commun 101445.
53. Shimizu Y, Kai S, Takao Y, Hyodo T, Egashira M (2000) Layered mesoporous SnO2 for effective ethanol detection at reduced working temperature. Sens. Actuators B Chem 65:349–357